ADVANCED MATERIALS TECHNOLOGIES
www.advmattechnol.de

Straining and Tuning Atomic Layer Nanoelectromechanical Resonators via Comb-Drive MEMS Actuators

Yong Xie, Jaesung Lee, Yanan Wang, and Philip X.-L. Feng**

Broad frequency tuning is an essential attribute desired in resonant nano/microelectromechanical systems (NEMS/MEMS) and their many applications. Endowed with ultrahigh intrinsic strain limits, combined with other unconventional properties, atomically thin 2D crystalline materials are excellent candidates for building highly tunable resonant NEMS. Here a heterogeneous integration approach is demonstrated to enable on-chip, continuous, and broad frequency tuning in 2D NEMS resonators by directly controlling strain via voltage-controlled silicon-on-insulator (SOI) comb-drive MEMS actuators. By varying the comb-drive actuation voltage, resonance frequency of the 2D NEMS can be tuned as large as 75% continuously with precise control. The comb-drive actuation-enabled direct straining and tuning also yield quality (*Q*) factor boost up to twofold. It is validated that this technique is readily applicable to straining and tuning representative 2D NEMS in various leading materials: graphene, molybdenum disulfide (MoS_2), and hexagonal boron nitride (h-BN). This study demonstrates that additively integrating 2D resonators atop mainstream SOI MEMS enables a versatile platform, and opens new possibilities for voltage control and broad tuning of 2D NEMS on chip.

1. Introduction

Manipulating strain levels in semiconducting crystals allows changing their band structures, providing opportunities for tailoring and finely tuning their electrical, optical, mechanical, and thermal properties. Strain engineering of mainstream semiconductors has already been widely exploited in the semiconductor industry to achieve desired device performance. In electronics, 0.55% tensile strain of Si channel, using SiGe-on-insulator substrates, can reduce effective mass of carriers hence boost mobility by 50%, and increase drive current by 80% compared to silicon-on-insulator (SOI) counterparts,[1,2] facilitating improvement of high-frequency responses in field-effect transistors (FETs). In optoelectronics, tensile uniaxial strain up to 2% has been employed to transform indirect bandgap into direct bandgap in multilayer WSe_2[3,4] to enhance optoelectronic conversion and quantum efficiency. Further, strain engineering has also been proposed for tuning and controlling solid-state spin qubits in wide bandgap materials, toward emerging quantum communication and computing applications.[5]

Strain engineering in 2D materials (e.g., graphene and transition metal dichalcogenides such as molybdenum disulfide (MoS_2)) is of special interest, also because of their superior strain limits compared to those of mainstream crystalline materials (e.g., Si, SiC, GaAs): breaking strain limit of 2D materials is as high as ≈25% for graphene and MoS_2,[6,7] much higher than for Si which breaks at strain level of 1.5%.[8] The remarkable strain resilience of 2D materials suggests exceptionally broad ranges of tuning and manipulating materials properties, promising new possibilities of building devices that have not only wide tunability, but also unconventional effects and performance that might emerge in the large strain regime.[9]

Various techniques have been developed and employed to introduce large strain in 2D materials. Among these techniques, transferring 2D materials onto flexible substrates and then bending and deforming bulk substrate has been commonly adopted to apply strain to substrate-supported 2D devices due to its simplicity of integration between 2D materials and flexible substrates.[3,4] This technique is convenient and useful for studying strain effects on material properties but largely relies on bulky external equipment to deform the structures. To control strain level in suspended 2D materials within the device platform, heterogeneously integrating 2D materials onto microelectromechanical systems (MEMS) have been attempted. Both electrostatic and thermal SOI MEMS actuators have been employed to attain high strain levels in 2D materials up to 10% for graphene,[10] 1.3% for MoS_2,[11] and 2.5% for $MoSe_2$,[12] and effects of staining on fundamental material properties are characterized using such MEMS platforms.

Among the diverse devices enabled by 2D materials, resonant nanoelectromechanical systems (NEMS) greatly benefit

Prof. Y. Xie, Dr. J. Lee, Dr. Y. Wang, Prof. P. X.-L. Feng
Department of Electrical Engineering & Computer Science
Case School of Engineering
Case Western Reserve University
Cleveland, OH 44106, USA
E-mail: yxie@xidian.edu.cn; philip.feng@ufl.edu
Prof. Y. Xie
Key Laboratory of Wide Band-Gap Semiconductor Technology
School of Advanced Materials and Nanotechnology
Xidian University
Xi'an 710071, China
Dr. J. Lee, Dr. Y. Wang, Prof. P. X.-L. Feng
Department of Electrical & Computer Engineering
Herbert Wertheim College of Engineering
University of Florida
Gainesville, FL 32611, USA
The ORCID identification number(s) for the author(s) of this article can be found under https://doi.org/10.1002/admt.202000794.

DOI: 10.1002/admt.202000794

from strain tuning and control. Mainstream NEMS and MEMS resonators (based on Si and other mature structural materials) are ubiquitous and pervasively employed in sensing, signal processing, and communication applications.[13] NEMS resonators based on atomically thin 2D materials such as graphene and MoS_2 have recently been demonstrated; and they exhibit new features and excellent device performance such as dynamic range up to ≈70–110 dB.[14] Resonance characteristics of NEMS devices with 2D materials strongly depend on built-in tension or strain levels, thus strain engineering can offer a broad range of tunability in their specifications and performance. In fundamental research, the ultralow mass density and the ultrahigh strain limit of 2D NEMS resonators promise intriguing pathways toward reaching unprecedented frequencies and tuning ranges. It is also highly attractive to cool these resonators to explore new phenomena in quantum regime. Toward potential applications in ultralow-power resonant signal processing and sensing, the exceptional tuning and voltage control capabilities, ultrahigh responsivities, combined with improving strain engineering and quality (Q) factor enhancement, also present technologically compelling perspectives for systematically investigating 2D NEMS.[15] The strain level in as-fabricated 2D NEMS resonators can reach the range of 30–180ppm (wet transfer),[16,17] 340 ppm (dry transfer),[18] 40–900 ppm (exfoliated 2D materials on top of SiO_2).[19–21] Based on the theoretical prediction, if we achieve strain engineering up to 1%, it could give rise to frequency tuning range, $\Delta f/f_0 = (f - f_0)/f_0$, from 230% to 1700%, enabling highly tunable NEMS resonators with unprecedented tuning range. To date, frequency tuning of 2D NEMS resonators is predominantly achieved by applying electrostatic forces in the devices. The frequency tuning range attainable by the electrostatic method, however, is limited by pull-in induced failure, or capacitive softening or stiffening. Also, it deteriorates the Q factor as a consequence of considerable energy dissipation (loaded Q effect). In contract, frequency tuning induced by uniaxial straining using a MEMS actuator does not suffer from electrostatic pull-in, capacitive softening, and loaded Q effect, potentially provides much wider frequency tuning range without compromising other important device characteristics. Despite the successful demonstrations of applying large strain up to 10% using MEMS actuators on 2D materials for probing strain effects on material properties, the reported frequency tuning range in 2D NEMS resonators strained by MEMS actuators is only $\Delta f/f_0 \approx 0.017\%$ at low temperature,[22] which is far lower than expectations. Such discrepancy between the promises of strain engineering of 2D materials and the realistic specifications of the strained 2D NEMS devices is intriguing and remains largely unexplored so far.

To close the technical gap, here we investigate frequency tuning of 2D NEMS resonators at room temperature by integrating 2D NEMS resonators onto SOI comb-drive MEMS actuators, across several orders of magnitude in length scale. We fabricate bi-layer to four-layer (2L to 4L) semiconducting MoS_2, as well as few-layer semimetal graphene and multilayer insulating hexagonal boron nitride (h-BN) NEMS resonators, and investigate their frequency tuning by carefully controlling in-plane uniaxial strain via comb-drive MEMS actuators. We achieve frequency tuning as high as 75%, which is more than three orders of magnitude higher than the reported values using a similar method.[22] In addition to frequency tuning, we also find that our method can enhance Q factor of the resonators by increasing strain thus resonance frequency, rendering a new way to improving Qs of 2D NEMS resonators.

2. Results and Discussions

Figure 1a shows the schematic of a 2D MoS_2 NEMS resonator integrated onto a comb-drive actuator. The comb-drive is actuated by applying a direct current (dc) polarization voltage (V_{dc}), and the electrostatic force introduces an in-plane uniaxial strain to the suspended 2D crystal. As 2D crystals are thinned down to few-layer thickness, with sufficient built-in tension, the device characteristics fall into the membrane regime.[23] In the membrane regime, the resonance frequency of 2D NEMS resonator is determined by the strain/tension rather than flexural rigidity, hence the resonance frequency of 2D device can be efficiently tuned by the external force from the comb-drive actuator (Figure 1b). The device resonance is photothermally excited and detected by a customized laser interferometry system as shown in Figure 1c (see the Experimental Section for more details).

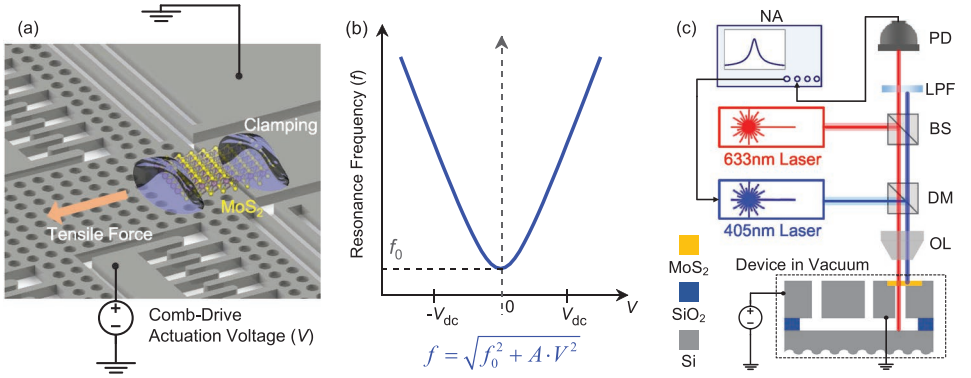

Figure 1. Illustration of a 2D NEMS resonator integrated onto a single-crystal SOI comb-drive MEMS actuator. a) Device configuration of the comb-drive actuator with the suspended 2D crystal (e.g., MoS_2). b) Frequency tuning (f versus V_{dc}) curve in NEMS resonator via comb-drive actuator straining. c) Illustration of optical interferometry system. NA, PD, LPF, BS, DM, and OL denote network analyzer, photodetector, longpass filter, beam splitter, dichroic mirror, and objective lens, respectively. All measurements are performed in moderate vacuum (≈20 mTorr) at room temperature.

We first integrate a 2D NEMS resonator onto a specially designed SOI comb-drive actuator (**Figure 2**). As shown in Figures 1 and 2, a microtrench or gap (typical gap width of ≈1.5 to 3 µm) is designed between a convex edge on the stationary pad and a movable pad (with etching holes for release) with comb-drive electrostatic actuation, where 2D crystals will be additively integrated and suspended over the microtrench to enable 2D resonators, via a precisely aligned transfer process. The comb-drive actuator is fabricated using a conventional SOI MEMS fabrication method. A SOI wafer, with 12 µm thick silicon (Si) and 2 µm thick SiO_2, is employed as the substrate. After the deep reactive ion etching (DRIE) of the 12 µm thick top Si layer (Figure 2a), few-layer MoS_2, graphene or h-BN flakes are exfoliated and transferred onto the microtrench in the comb-drive actuator by an all-dry transfer process (Figure 2b).[24] Subsequently, we remove the 2 µm thick buried oxide (BOX) using buffered oxide etch (BOE) followed by critical point drying (CPD) to release the comb-drive actuator. The MEMS fabrication procedure is compatible with the commercially available SOI MUMPs process, which makes the design appealing in scalable fabrication applications with small modifications.[25] To prevent any sliding between the 2D device and the Si comb-drive during strain tuning, 2D device is clamped by epoxy droplets on both ends of the flakes (Figure 2c). Details of the process can be found in the Experimental Section and Figure S2 in the Supporting Information. The photoluminescence (PL) and Raman signatures of the transferred 2D materials on the comb-drive actuator are measured before and after the comb-drive releasing process to confirm the crystal quality and the number of layers of the suspended 2D crystals (Figure S3, Supporting Information).

The built-in strain can strongly influence the frequency tuning behavior (i.e., tuning range and lineshape) of 2D resonators;[19,26] hence we have examined the evolution of built-in tension of 2D resonators at each fabrication step. Figure 2e shows the fundamental resonance frequency ($f \approx 16.7$ MHz) of a MoS_2 resonator (Device A, with thickness $t = 3.0$ nm, length $L = 2$ µm and width $w = 2.7$ µm) with $Q \approx 67$. After the release of the comb-drive, the resonance frequency of the MoS_2 resonator decreases as shown in Figure 2d. The spring constant (12 N m^{-1}) of the comb-drive actuator is designed to be comparable or lower compared to the in-plane stiffness of the 2D NEMS device, $k_{2D} = E_Y wt\, L^{-1}$ (10–200 N m^{-1}), where E_Y is Young's modulus [N m^{-2}]. Accordingly, after the release of the comb-drive actuator, it becomes movable, and the NEMS–MEMS forms a coupled system, which assumes a new equilibrium condition based on the balance of the stiffness of the comb-drive actuator and 2D membrane, relaxing the tension in the MoS_2 resonator thus lowering its frequency. The fundamental-mode resonance frequency of the MoS_2 resonator after the comb-drive MEMS release is

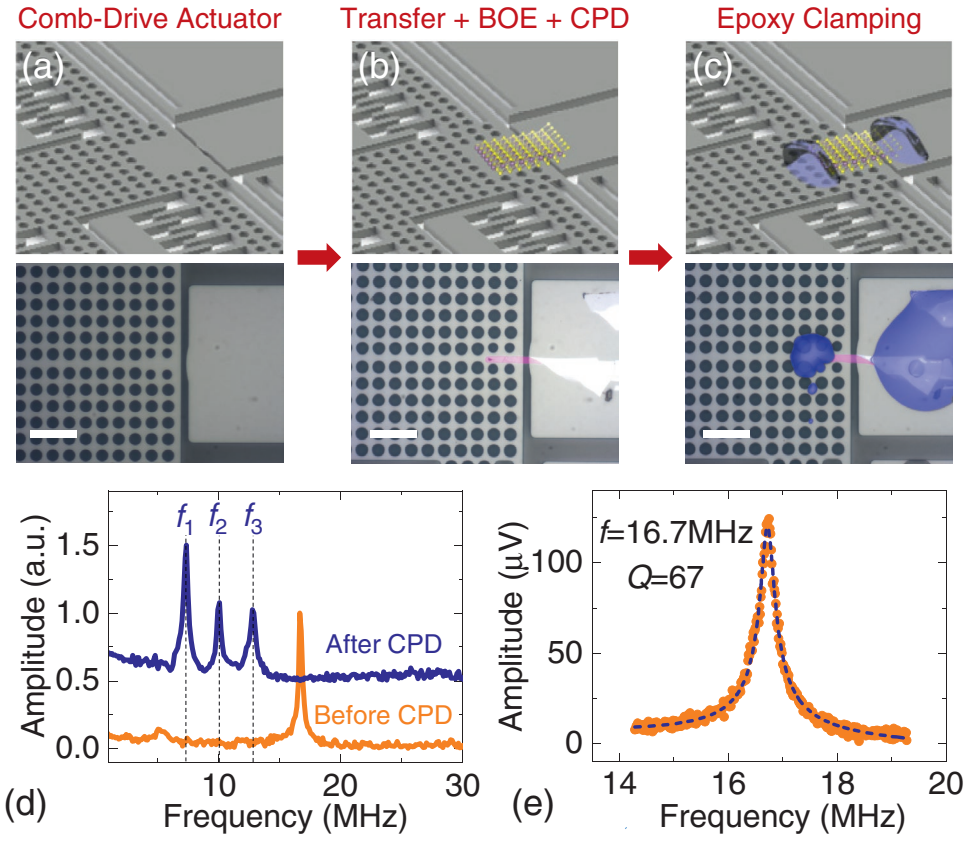

Figure 2. Schematic of the device fabrication process and initial device characterization. a) SOI comb-drive actuator. b) Transferring MoS_2 onto the comb-drive followed by buffered oxide etch (BOE) and critical point drying (CPD) to release the top Si device layer from the SOI wafer. c) Secure clamping by applying epoxy droplets at both ends of the MoS_2 flake using a micropipette integrated with a micropositioner. a–c) Scale bars are 20 µm. d) Resonant frequencies measured before and after CPD. e) Fundamental-mode resonance in (d) before CPD.

measured to be $f_1 = 7.3$ MHz, with $Q_1 = 31$, over two times lower than measured before the comb-drive release. The resonance frequency of the second mode is observed at $f_2 = 10.0$ MHz, with $Q_2 = 42$. The resonance frequency of the third mode is observed at $f_3 = 12.9$ MHz, with $Q_3 = 38$. To further understand measured multimode resonances, we have performed finite element simulation (FEM) (Section S4, Supporting Information). The frequency ratios of the second and third mode to the first mode are $f_2/f_1 = 1.37$, $f_3/f_1 = 1.77$, respectively, which prove the 2D resonator is operating in the membrane regime and the resonant frequency is dominated by built-in tension (Section S4, Supporting Information). The fundamental-mode resonant frequency (f) of the device can be calculated by

$$f = \frac{1}{2L}\sqrt{\frac{\gamma}{\rho t}} = \frac{1}{2L}\sqrt{\frac{E_Y \varepsilon}{\rho}} \tag{1}$$

where L, γ, E_Y, ρ, ε denotes the length, 2D tension [N m^{-1}], Young's modulus [N m^{-2}], volume mass density [kg m^{-3}], and strain of the 2D NEMS. When there is no external force, the initial built-in tension γ_0 [N m^{-1}] of the device is

$$\gamma_0 = \frac{8 f_0^2 L m_{\text{eff}}}{w} \tag{2}$$

where f_0, w, and m_{eff} denote resonant frequency without external force, width, and effective mass of 2D NEMS. For the doubly clamped rectangular membrane, $m_{\text{eff}} = 0.5 m_0$ ($m_0 = \rho L w t$ is the static mass of the 2D device) for the lowest mode (Section S5, Supporting Information).[27] From Equation (2), we find that the built-in tension is reduced from 0.677 to 0.129 N m^{-1} after comb-drive release. The Q factor of the MoS_2 resonator is also decreased from 67 to 31 after comb-drive release, suggesting that tension plays an important role in overcoming damping and maintaining Q factor of the 2D resonator.

We then focus on using the fully released comb-drive actuator to tune the frequency of the MoS_2 NEMS while measuring its resonance characteristics. **Figure 3**a shows an optical microscope image of a 3L MoS_2 device (Device B) with length $L = 2$ µm and width $w = 4.3$ µm before applying epoxy anchoring patches for secure clamping (the fabrication process of this device is shown in Figure S5, Supporting Information). The PL spectrum of the MoS_2 flake exhibits an indirect transition peak at ≈1.45 eV, verifying it is 3L MoS_2.[28] The Raman spectrum shows a separation wavenumber of 23 cm^{-1} between E' and A' peaks (Figure 3c), also confirming the 3L features of the MoS_2 flake.[29] The device exhibits the tunable resonance upon varying the actuation voltage of the comb-drive MEMS. For the 3L MoS_2 device (Device B), the resonance frequency is symmetrically shifted up from 8.2 to 14.6 MHz as the actuation voltage is swept from 0 to 18 V (or –19 V), showing frequency tuning range of $\Delta f/f_0 \approx 75\%$. We note that this measured tuning range is ≈5000 times larger than the reported value attained by comb-drive tuning.[22] This large frequency tuning range is attributed to the effective modification of strain in 2D devices by using specially designed microtrenches on the comb-drive actuators, where range of trench or gap width (≈1.5 to 3 µm) is chosen considering fabrication yield of atomically thin suspended devices.

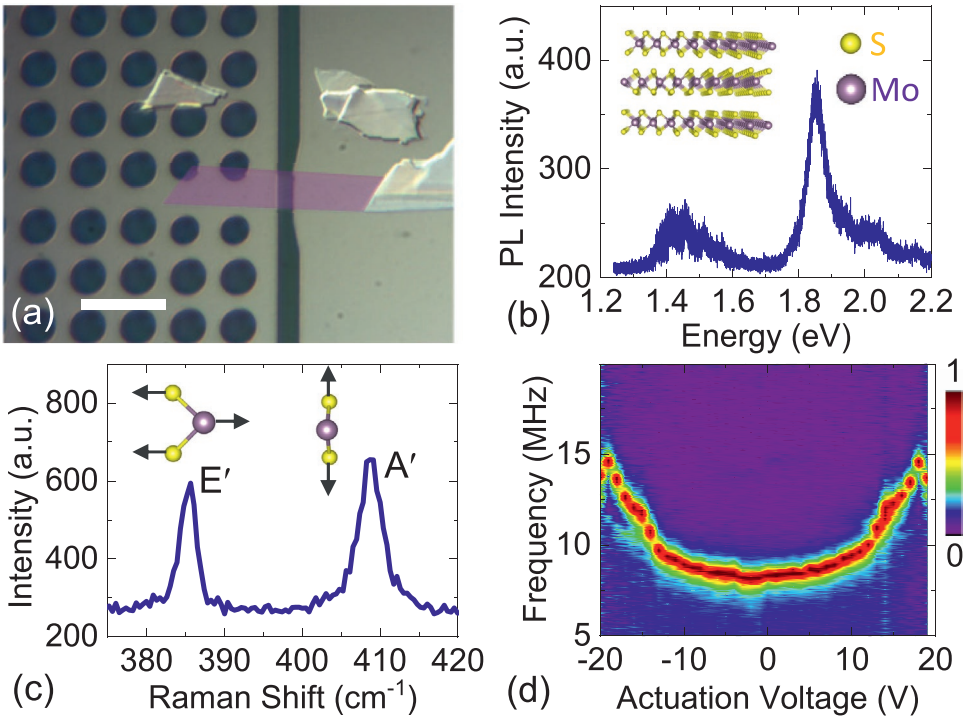

Figure 3. Resonance characterization and frequency tuning of 3L MoS_2 resonator. a) Optical microscope image of a 3L MoS_2 NEMS resonator on a SOI comb-drive actuator. Scale bar: 10 µm. b) PL and c) Raman spectra of the suspended MoS_2 membrane, respectively. d) Color (normalized amplitude) map plot of measured frequency tuning of the MoS_2 resonator with varying comb-drive actuation voltage.

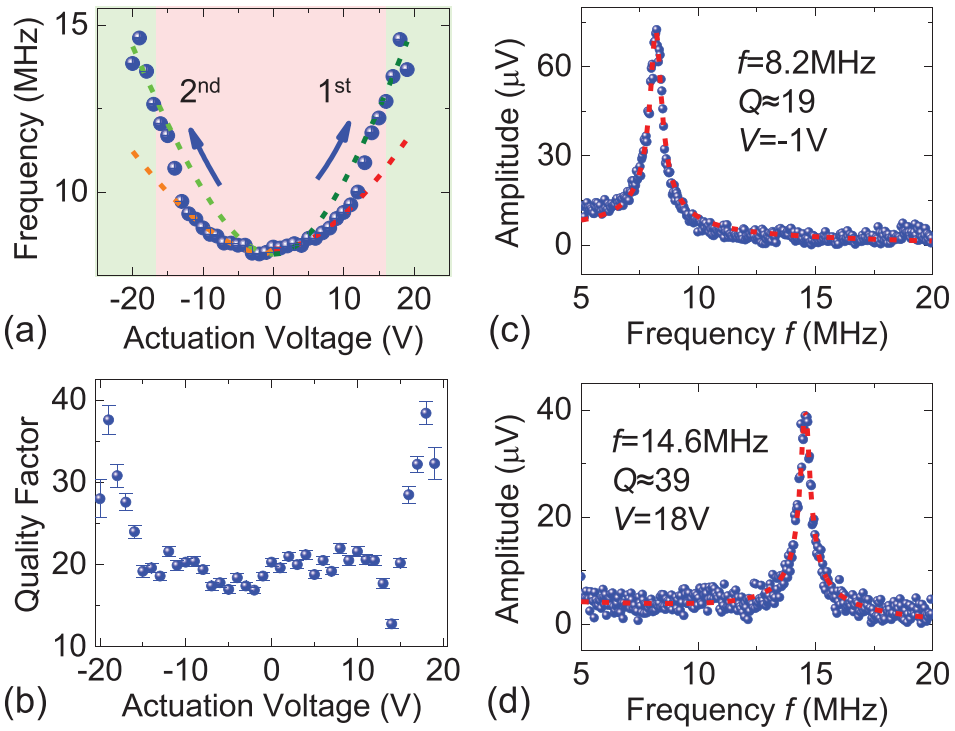

Figure 4. Strain tuning of a 3L MoS_2 NEMS resonator. a) Frequency shift and b) evolution of quality (Q) factor versus comb-drive actuation voltage V_{dc}, respectively, measured from the device shown in Figure 3a (Device B). Orange, red, light green and dark green dashed lines in (a) show fitting measured frequency tuning curves in $-13\ V < V_{dc} < 0\ V$, $0\ V < V_{dc} < 13\ V$, $-18\ V < V_{dc} < -13\ V$ and $13\ V < V_{dc} < 18\ V$ to Equation (5), respectively. The light pink and light green background colors in (a) represent different fitting regimes. Resonances of Device B under comb-drive actuation voltage of c) $V_{dc} = -1\ V$ and d) $V_{dc} = 18\ V$.

To comprehensively understand the frequency tuning behavior and coupling mechanism between the 2D resonators and comb-drive actuator, we pursue analytical modeling to compare with experimental measurement. The evolution of f and Q of the 3L MoS_2 device versus the comb-drive actuation voltage (V_{dc}) is shown in **Figure 4**. Considering additional tension induced by the comb-drive MEMS actuator upon application of V_{dc}, the resonance frequency becomes

$$f = \frac{1}{2}\sqrt{\frac{\gamma_0 w + F(V_{dc})}{2Lm_{eff}}} \tag{3}$$

where $F(V_{dc})$ is the force induced by the comb-drive actuator at V_{dc}. When V_{dc} is set to be 0 V, $F(V_{dc})$ is zero, and the initial built-in tension could be calculated by Equation (2), then we can determine the γ_0 from Device B as 0.1 N m^{-1}. The force generated by the comb-drive actuator can be expressed as

$$F(V_{dc}) = \eta N \frac{\epsilon h}{d} V_{dc}^2 \tag{4}$$

where N, ϵ, h, d and η denotes the number of comb teeth, vacuum permittivity, thickness ($h \approx 12$ μm), and comb finger gap ($d \approx 3$ μm) of the SOI MEMS comb-drive actuator, and the efficiency of the force applied to 2D materials. The different η could be attributed to various factors including additional device mass from fabrication residues and in-plane stiffness of 2D materials. From Equations (3) and (4), we can derive the relationship between the comb-drive voltage V_{dc} and the resonant frequency (f) of 2D NEMS device as

$$f = \sqrt{f_0^2 + \frac{\eta N \epsilon h}{8Lm_{eff}d} V_{dc}^2} \tag{5}$$

We fit the strain tuning curve shown in Figure 4a to Equation (5). From the fitting (dash curves in Figure 4a), we find two different regimes. In the lower $|V_{dc}|$ regime, the fitting gives a force efficiency η of $\eta \approx 0.23$ for $-13\ V < V_{dc} < 0\ V$ (orange dashed lines in Figure 4a) and $\eta \approx 0.31$ for $0\ V < V_{dc} < 13\ V$ (red dashed lines in Figure 4a). With the higher $|V_{dc}|$, we find $\eta \approx 0.55$ for $-18\ V < V_{dc} < -13\ V$ (light green dashed lines in Figure 4a), and $\eta \approx 0.65$ for $13\ V < V_{dc} < 18\ V$ (dark green dashed lines in Figure 4a). In suspended 2D materials, ripples are frequently observed[30,31] and it could change elastic properties of the 2D materials.[31] With an applied voltage, tensile strain tends to modify structure of ripples in 2D materials, accordingly, η is increased from 0.23 to 0.55 (negative V_{dc}) and 0.31 to 0.65 (positive V_{dc}), showing the larger frequency tuning rate in $13\ V < |V_{dc}| < 18\ V$. It is worth noting that the Q of MoS_2 resonator is clearly improved beyond $|V_{dc}| > 15\ V$, where it shows significant changes of η in the frequency tuning measurements. Although the energy dissipation mechanisms in 2D NEMS resonators are still largely unexplored, the observed Q enhancement could be related to modification of the ripples in the 2D material. Further, the observed Q enhancement by tensile straining has also been reported earlier in conventional

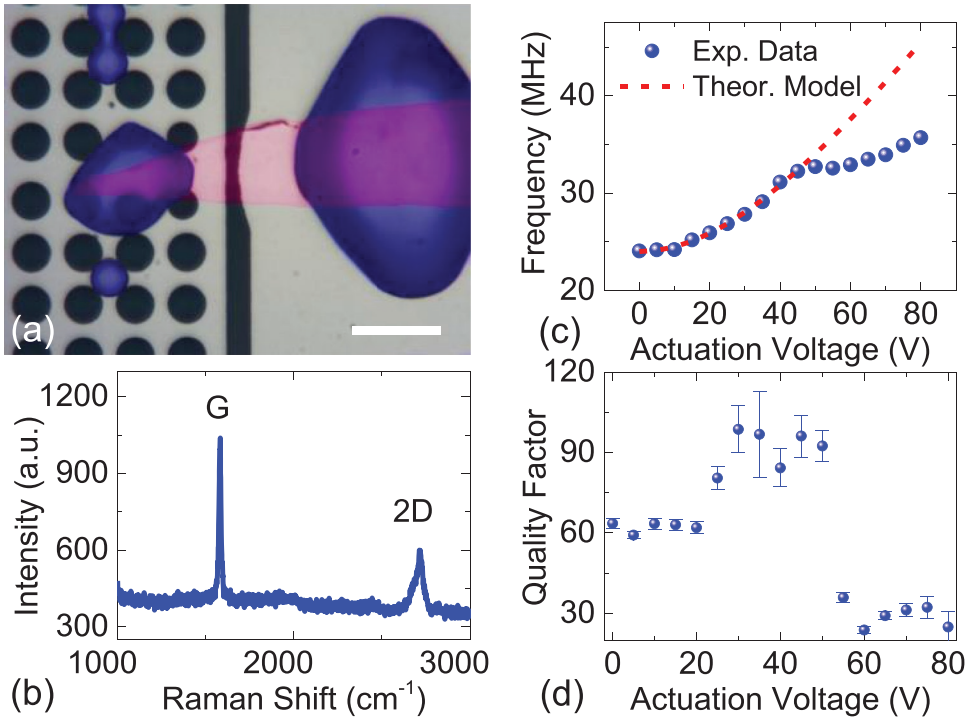

Figure 5. Strain tuning of multilayer graphene NEMS resonator. a) Optical image of Device C. Scale bar: 10 µm. b) High-quality multilayer graphene in (a) confirmed by Raman spectroscopy. c) Frequency tuning of the graphene resonator controlled by an SOI comb-drive actuator. d) Quality factor tuning measured in the graphene resonator.

NEMS and MEMS resonators.[32,33] Previous experiments on strained Si_3N_4 strings reveal that increase of Q factor could be attributed to either reduced internal material damping[34] or increased elastic energy.[35] Another possible reason is that here the 2D resonators and comb-drive MEMS form coupled systems, for which the coupling rate might depend on the tensile strain.[36] More detailed explanations will deserve further investigations and future work.

An interesting phenomenon is that above certain actuation voltage strength ($|V_{dc}|$ >18 V in Figure 4a,b), the resonant frequency and the Q factor start to drop at the same time. This is an indicator that the MoS_2 crystal starts to slide on top of the SOI MEMS actuator. We believe the Q factor drop at high actuation voltage is due to the slippage issue instead of deterioration. According to earlier studies on in situ straining of multilayer graphene,[37,38] the fracture strain could be above 20% for multilayer graphene. The maximum strain we have achieved here is 0.013% for 3L MoS_2 NEMS (Device B), which is still far from the maximum strain that can be applied to such 2D materials. This also explains the earlier observation that there is nearly no Raman G peak split with the applied 10% strain using a MEMS actuator,[10] indicating sliding could happen in such systems and under certain conditions. In Figure 4a, it is shown that after the first voltage (V_{dc}) sweep of frequency tuning measurement (marked with the "first" arrow), the resonant frequency of MoS_2 NEMS decreases slightly from 8.3 to 8.2 MHz (Figure 4b) at $V_{dc} = 0$ V.

To validate the general applicability and flexibility of this on-chip straining and tuning platform, we perform strain tuning of multilayer graphene NEMS resonators on an SOI MEMS actuator, as demonstrated in **Figure 5**. Figure 5a shows an optical microscope image of a 3 nm thick graphene device (Device C) with length $L = 1.4$ µm and width $w = 7$ µm. Raman spectroscopy result shows the high quality of the exfoliated graphene on the actuator (Figure 5b). A similar trend of tuning is observed in the multilayer graphene device shown in Figure 5c,d. The frequency keeps increasing with increasing V_{dc}. We employ Equation (5) to fit the strain tuning curve, which matches the data very well for $V_{dc} < 45$ V. As the actuation voltage increases to be above a threshold voltage, $V_{dc} > 45$ V in Figure 5c, the resonant frequency almost saturates first and then increases again, albeit at a lower rate as V_{dc} continues to increase. This clear cross-over point at which the frequency tuning rate df/dV_{dc} jumps is an indicator of sliding of graphene NEMS on the SOI comb-drive. The same as earlier observed in atomically thin MoS_2 resonators, the Q factor of the graphene resonator first increases with increasing V_{dc} (from 20 to 40 V in Figure 5d). At $V_{dc} > 45$ V, the Q factor drops to one-third of the highest value.

Further, we extend this chip-scale strain engineering platform to investigate 2D resonators built upon another very important 2D material, hexagonal boron nitride (h-BN). As an insulator, h-BN has no free carriers, and thus h-BN 2D resonators are highly challenging to be tuned by using traditional electrostatic gating methods.[39] Here, we demonstrate the universal applicability of the present comb-drive MEMS tuning platform as shown in **Figure 6**. Figure 6a shows an optical microscope image of a 20 nm thick h-BN device (Device D) with length $L = 1.4$ µm and width $w = 7$ µm. Raman spectroscopy shows the high quality of the exfoliated h-BN on the actuator (Figure 6b). Beam theory can be invoked to model the h-BN

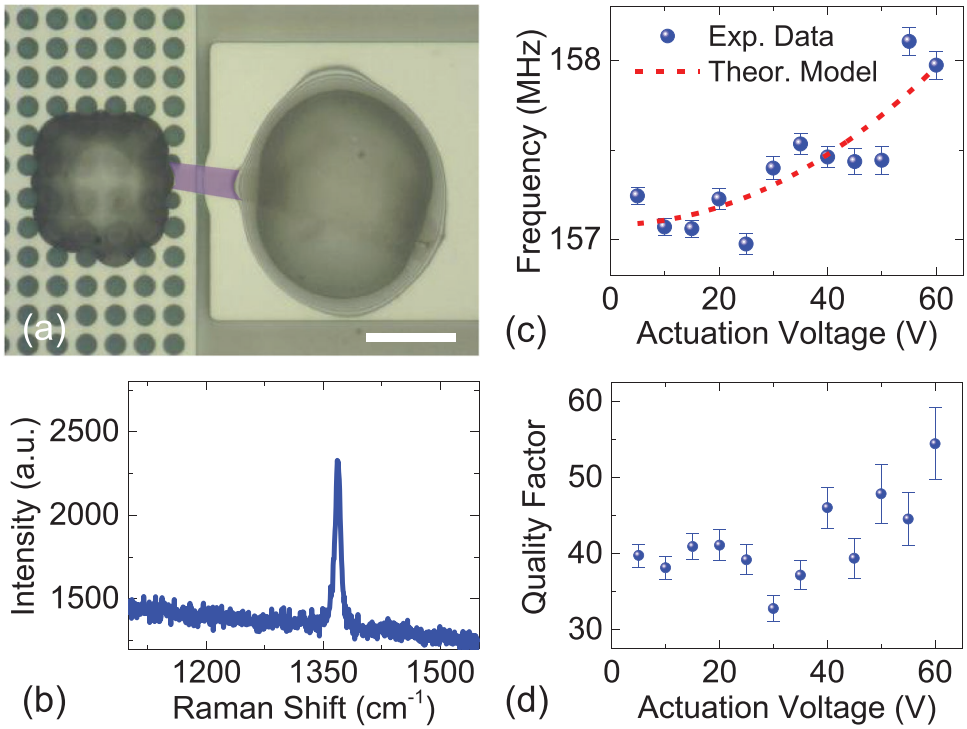

Figure 6. Strain tuning of a multilayer h-BN NEMS resonator. a) Optical image of Device D. Scale bar: 10 µm. b) High-quality multilayer h-BN in (a) confirmed by Raman spectroscopy. c) Frequency tuning of h-BN resonator by SOI comb-drive actuator. d) Quality factor tuning of h-BN resonator.

nanomechanical devices.[40] Equation (5) can still be used to fit the voltage tuning results in Figure 6c. With proper actuation voltage (up to 60 V in Figure 6d), the Q factor increases from 33 to 55, which is still in consistence with the observations in MoS_2 and graphene NEMS.

Our platform utilizes a practical strategy to control the initial strain variance, thus can be readily adopted for solving the reproducibility of resonant frequency from device to device or determine the tuning coefficient, which is strongly influenced by initial strain.[41] Toward future on-chip, low-voltage integration, the actuation voltage can be further reduced, by increasing the thickness of the SOI device layer (h) and the comb-drive teeth number N, or reducing the comb finger gap d. In addition, other schemes with special MEMS designs could also be adopted to amplify the force generated by comb-drive actuator to further reduce the actuation voltage to apply the same force for stretching the 2D device. With further engineering of the transfer of chemical vapor deposited (CVD) graphene or MoS_2,[42,43] the concept of straining and tuning can be extended to wafer scale. By integrating local gate, vibrating channel transistors could be utilized for on-chip integration.[44] Further, by integrating graphene on h-BN to provide excellent electronic transduction, it would be feasible to realize electrical readout of h-BN NEMS.[45] As the Q factors of 2D resonators could be improved dramatically at low temperatures,[46] the highly doped device layer of SOI also help guarantees the improved device reliability and relevant performance. In addition, our design of comb-drive MEMS actuator is compatible with low temperature experiments, which is readily useful to probe quantum phenomena at very low temperatures.[47]

3. Conclusion

In conclusion, we have demonstrated wide frequency tuning and Q enhancement of 2D resonators by precisely controlling strain applied on 2D crystals using SOI comb-drive MEMS actuators. Facilitated by an all-dry transfer method, vibrating 2D NEMS are successfully integrated onto comb-drive MEMS actuators, demonstrating additive heterogeneous integration across several orders of magnitude in length scale. By controlling the actuation voltage of the comb-drive MEMS, the frequency of the 2D resonators has been tuned up as large as 75%. In addition, Q factors of the 2D resonators have also gained a boost of two times. The demonstration in this work suggests the comb-drive MEMS actuators can serve as a universal platform for continuously straining 2D materials and NEMS. This has rendered new findings and understating of 2D NEMS–MEMS hybrid integration, revealing a viable approach to on-chip control and engineering of 2D materials and devices additively manufactured onto mainstream technologies.

4. Experimental Section

Fabrication of Single-Crystal SOI Comb-Drive MEMS Actuators: The comb-drive MEMS actuators were fabricated on a 4 in. SOI wafer with a top Si device layer of 12 µm and an underneath oxide layer (SiO_2) with thickness of 2 µm. The structure of comb-drive actuator was defined by lithographical patterning. The top Si layer without the protection of photoresist was etched away by a Bosch process using DRIE. The wafer was then diced into 5 mm × 5 mm chips.

Fabrication of Suspended 2D Materials onto Comb-Drive Actuator: 2D materials were first exfoliated onto PDMS stamps. Then suitable 2D

flakes (e.g., MoS_2 with length larger than 10 µm, thinner than five layers) were chosen and transferred, with precise alignment, onto the convex edge region of the microtrenches. The SiO_2 layer underneath the comb-drive actuator was then removed in BOE solution and then the chips were released in a CPD to prevent stiction to the bottom Si handle layer. To secure the clamping and prevent slipping of the 2D devices with respect to the comb-drive actuator, microdroplets of epoxy were applied on both ends of the 2D devices using a tapered quartz micropipette, whose positions were controlled by an XYZ stage with sub-micrometer resolution.

Interferometric Resonance Measurements: The resonance characteristics of the 2D devices were measured by using an ultrasensitive optical interferometry system. The resonance of the device was excited using an amplitude modulated 405 nm blue laser, and was detected using a 633 nm red laser. The laser power was adjusted to be below 200 µW to avoid laser heating. In addition, the blue laser spot was parked on the supported region and kept at minimal power to minimize heating of the 2D NEMS. Before and during the tuning experiments, the laser power was calibrated and the resonant frequency was monitored to make sure the frequency tuning was only induced by the comb-drive actuator. The typical laser spot size was ≈1 µm for the 633 nm laser. The output signal from the photodetector was recorded by a network analyzer. A Keithley source measure unit (SMU) was employed to apply DC actuation voltage (V_{dc}) to the MEMS actuator.

Raman Scattering and Photoluminescence Measurements: 2D NEMS were preserved in a vacuum chamber and Raman and PL responses were measured using a customized micro-Raman system. During the measurement, a 532 nm laser was used, focusing upon the center of the 2D NEMS device. The spot size of laser was ≈1 µm. Raman scattering signal from the sample was collected in a backscattering geometry and then guided to a spectrometer (Horiba iHR550). Raman signal was recorded using a liquid-nitrogen-cooled CCD. PL spectra were recorded using the same spectrometer and CCD. The typical integration time was 10 s for PL and 60 s for Raman measurements, respectively.

Supporting Information

Supporting Information is available from the Wiley Online Library or from the author.

Acknowledgements

Financial support from the National Science Foundation (NSF) CCSS Grant (ECCS-1509721) and the National Natural Science Foundation of China (NSFC) Grant (No. 61704129) is acknowledged. Y.X. thanks financial support from the China Scholarship Council (CSC, under Award No. 201706965048) during his visit at Case Western Reserve University. Y.X. thanks Hao Jia (Case Western Reserve University), Xiaohua Ma (Xidian University), and Heng Xiong and Haobin Niu (FACRI) for helpful discussions and technical support in the comb-drive MEMS actuator fabrication.

Conflict of Interest

The authors declare no conflict of interest.

Author Contributions

Y.X. and J.L. contributed equally to this work. Y.X., J.L. and P.F. conceived and designed the experiments. Y.X. fabricated the devices. Y.X., J.L., and Y.W. carried out the device characterization with technical support from P.F. Y.X., J.L., and P.F. analyzed the data and wrote the manuscript. All authors reviewed and commented on the manuscript. P.F. supervised the project.

Keywords

2D materials, comb-drive, nanoelectromechanical systems, resonator, strain engineering

Received: August 11, 2020
Revised: November 7, 2020
Published online: December 11, 2020

[1] M. Chu, Y. Sun, U. Aghoram, S. E. Thompson, *Annu. Rev. Mater. Res.* **2009**, *39*, 203.
[2] S. W. Bedell, A. Khakifirooz, D. K. Sadana, *MRS Bull.* **2014**, *39*, 131.
[3] S. B. Desai, G. Seol, J. S. Kang, H. Fang, C. Battaglia, R. Kapadia, J. W. Ager, J. Guo, A. Javey, *Nano Lett.* **2014**, *14*, 4592.
[4] W. Wu, J. Wang, P. Ercius, N. C. Wright, D. M. Leppert-Simenauer, R. A. Burke, M. Dubey, A. M. Dongare, M. T. Pettes, *Nano Lett.* **2018**, *18*, 2351.
[5] Y.-I. Sohn, S. Meesala, B. Pingault, H. A. Atikian, J. Holzgrafe, M. Gündoğan, C. Stavrakas, M. J. Stanley, A. Sipahigil, J. Choi, M. Zhang, J. L. Pacheco, J. Abraham, E. Bielejec, M. D. Lukin, M. Atatüre, M. Lončar, *Nat. Commun.* **2018**, *9*, 2012.
[6] C. Lee, X. Wei, J. W. Kysar, J. Hone, *Science* **2008**, *321*, 385.
[7] S. Bertolazzi, J. Brivio, A. Kis, *ACS Nano* **2011**, *5*, 9703.
[8] S. E. Thompson, G. Sun, Y. S. Choi, T. Nishida, *IEEE Trans. Electron Devices* **2006**, *53*, 1010.
[9] M. G. Harats, J. N. Kirchhof, M. Qiao, K. Greben, K. I. Bolotin, *Nat. Photonics* **2020**, *14*, 324.
[10] H. H. Pérez Garza, E. W. Kievit, G. F. Schneider, U. Staufer, *Nano Lett.* **2014**, *14*, 4107.
[11] J. W. Christopher, M. Vutukuru, D. Lloyd, J. S. Bunch, B. B. Goldberg, D. J. Bishop, A. K. Swan, *J. Microelectromech. Syst.* **2019**, *28*, 254.
[12] Y. Yang, X. Li, M. Wen, E. Hacopian, W. Chen, Y. Gong, J. Zhang, B. Li, W. Zhou, P. M. Ajayan, Q. Chen, T. Zhu, J. Lou, *Adv. Mater.* **2017**, *29*, 1604201.
[13] O. Brand, I. Dufour, S. M. Heinrich, F. Josse, *Resonant MEMS*, Wiley, Weinheim **2015**, pp. 327–472.
[14] J. Lee, Z. Wang, K. He, R. Yang, J. Shan, P. X.-L. Feng, *Sci. Adv.* **2018**, *4*, eaao6653.
[15] P. X.-L. Feng, *Proc. of the 33rd IEEE Int. Conf. on Micro Electro Mechanical Systems (MEMS 2020)*, IEEE, Vancouver, Canada **2020**, pp. 212–217, https://doi.org/10.1109/MEMS46641.2020.9056243.
[16] R. A. Barton, I. R. Storch, V. P. Adiga, R. Sakakibara, B. R. Cipriany, B. Ilic, S. P. Wang, P. Ong, P. L. McEuen, J. M. Parpia, H. G. Craighead, *Nano Lett.* **2012**, *12*, 4681.
[17] R. De Alba, F. Massel, I. R. Storch, T. S. Abhilash, A. Hui, P. L. McEuen, H. G. Craighead, J. M. Parpia, *Nat. Nanotechnol.* **2016**, *11*, 741.
[18] N. Morell, A. Reserbat-Plantey, I. Tsioutsios, K. G. Schadler, F. Dubin, F. H. L. Koppens, A. Bachtold, *Nano Lett.* **2016**, *16*, 5102.
[19] C. Chen, S. Rosenblatt, K. I. Bolotin, W. Kalb, P. Kim, I. Kymissis, H. L. Stormer, T. F. Heinz, J. Hone, *Nat. Nanotechnol.* **2009**, *4*, 861.
[20] V. Singh, S. Sengupta, H. S. Solanki, R. Dhall, A. Allain, S. Dhara, P. Pant, M. M. Deshmukh, *Nanotechnology* **2010**, *21*, 165204.
[21] C. Samanta, N. Arora, K. Kumar V., S. Raghavan, A. K. Naik, *Nanoscale* **2019**, *11*, 8394.
[22] M. Goldsche, G. J. Verbiest, T. Khodkov, J. Sonntag, N. van de Driesch, D. Buca, C. Stampfer, *Nanotechnology* **2018**, *29*, 375301.
[23] J. Lee, Z. Wang, K. He, J. Shan, P. X.-L. Feng, *ACS Nano* **2013**, *7*, 6086.
[24] R. Yang, X. Zheng, Z. Wang, C. J. Miller, P. X.-L. Feng, *J. Vac. Sci. Technol. B* **2014**, *32*, 061203.
[25] http://www.memscap.com/products/mumps/soimumps, **2020**.
[26] T. Mei, J. Lee, Y. Xu, P. X.-L. Feng, *Micromachines* **2018**, *9*, 312.

[27] B. D. Hauer, C. Doolin, K. S. D. Beach, J. P. Davis, *Ann. Phys.* **2013**, *339*, 181.
[28] K. F. Mak, C. Lee, J. Hone, J. Shan, T. F. Heinz, *Phys. Rev. Lett.* **2010**, *105*, 136805.
[29] H. Li, Q. Zhang, C. C. R. Yap, B. K. Tay, T. H. T. Edwin, A. Olivier, D. Baillargeat, *Adv. Funct. Mater.* **2012**, *22*, 1385.
[30] J. C. Meyer, A. K. Geim, M. I. Katsnelson, K. S. Novoselov, T. J. Booth, S. Roth, *Nature* **2007**, *446*, 60.
[31] R. J. T. Nicholl, H. J. Conley, N. V. Lavrik, I. Vlassiouk, Y. S. Puzyrev, V. P. Sreenivas, S. T. Pantelides, K. I. Bolotin, *Nat. Commun.* **2015**, *6*, 8789.
[32] G. Cagnoli, J. Hough, D. DeBra, M. M. Fejer, E. Gustafson, S. Rowan, V. Mitrofanov, *Phys. Lett. A* **2000**, *272*, 39.
[33] J. M. L. Miller, A. Ansari, D. B. Heinz, Y. Chen, I. B. Flader, D. D. Shin, L. G. Villanueva, T. W. Kenny, *Appl. Phys. Rev.* **2018**, *5*, 041307.
[34] S. Schmid, K. D. Jensen, K. H. Nielsen, A. Boisen, *Phys. Rev. B* **2011**, *84*, 165307.
[35] Q. P. Unterreithmeier, T. Faust, J. P. Kotthaus, *Phys. Rev. Lett.* **2010**, *105*, 027205.
[36] G. J. Verbiest, D. Xu, M. Goldsche, T. Khodkov, S. Barzanjeh, N. van de Driesch, D. Buca, C. Stampfer, *Appl. Phys. Lett.* **2016**, *109*, 143507.
[37] C. H. Cao, S. Mukherjee, J. Y. Howe, D. D. Perovic, Y. Sun, C. V. Singh, T. Filleter, *Sci. Adv.* **2018**, *4*, eaao7202.
[38] P. Li, K. Cao, C. Jiang, S. Xu, L. Gao, X. Xiao, Y. Lu, *Nanotechnology* **2019**, *30*, 475708.
[39] X.-Q. Zheng, J. Lee, P. X.-L. Feng, *Microsyst. Nanoeng.* **2017**, *3*, 17038.
[40] J. Lee, P. X.-L. Feng, *Proc. of the 2012 IEEE Int. Frequency Control Symp.*, Baltimore, MD, May **2012**, https://doi.org/10.1109/FCS.2012.6243742.
[41] G. Grosso, H. Moon, B. Lienhard, S. Ali, D. K. Efetov, M. M. Furchi, P. Jarillo-Herrero, M. J. Ford, I. Aharonovich, D. Englund, *Nat. Commun.* **2017**, *8*, 705.
[42] H. Arjmandi-Tash, A. Allain, Z. Han, V. Bouchiat, *2D Mater.* **2017**, *4*, 025023.
[43] Y. Xie, Z. Wang, Y. Zhan, P. Zhang, R. Wu, T. Jiang, S. Wu, H. Wang, Y. Zhao, T. Nan, X. Ma, *Nanotechnology* **2017**, *28*, 084001.
[44] R. Yang, C. Chen, J. Lee, D. A. Czaplewski, P. X.-L. Feng, *Proc. of the 30th IEEE Int. Conf. on Micro Electro Mechanical Systems (MEMS 2017)*, IEEE, Piscataway **2017**, pp. 163–166, https://doi.org/10.1109/MEMSYS.2017.7863366.
[45] M. Liao, L. Sang, T. Teraji, S. Koizumi, Y. Koide, *Adv. Mater. Technol.* **2019**, *4*, 1800325.
[46] N. Morell, A. Reserbat-Plantey, I. Tsioutsios, K. G. Schädler, F. Dubin, F. H. L. Koppens, A. Bachtold, *Nano Lett.* **2016**, *16*, 5102.
[47] M. González, P. Zheng, E. Garcell, Y. Lee, H. B. Chan, *Rev. Sci. Instrum.* **2013**, *84*, 025003.